Genomic profiling and associated B cell lineages delineate the efficacy of neoadjuvant anti-PD-1-based therapy in oesophageal squamous cell carcinoma

Hongyu Zhang,[a,e] Haoyu Wen,[a,e] Qiaoliang Zhu,[a,e] Yuchen Zhang,[a] Fengkai Xu,[a] Teng Ma,[a] Yifan Guo,[a] Chunlai Lu,[a] Xuelian Zhao,[b] Yuan Ji,[b] Zhiqiang Wang,[d] Yiwei Chu,[d] Di Ge,[a,*] Jie Gu,[a,**] and Ronghua Liu[c,***]

[a]Department of Thoracic Surgery, Zhongshan Hospital, Fudan University, Shanghai, 200032, China
[b]Department of Pathology, Zhongshan Hospital, Fudan University, 200032, Shanghai, China
[c]Fifth People's Hospital and Shanghai Key Laboratory of Medical Epigenetics, Institutes of Biomedical Sciences, Fudan University, 200032, Shanghai, China
[d]Department of Immunology, School of Basic Medical Sciences, Shanghai Key Laboratory of Medical Epigenetics and Metabolism, Institutes of Biomedical Sciences, Fudan University, Shanghai, 200032, China

eBioMedicine
2024;100: 104971
Published Online xxx
https://doi.org/10.1016/j.ebiom.2024.104971

Summary

Background Neoadjuvant chemoimmunotherapy has offered novel therapeutic options for patients with locally advanced oesophageal squamous cell carcinoma (ESCC). Depicting the landscape of genomic and immune profiles is critical in predicting therapeutic responses.

Methods We integrated whole-exome sequencing, single-cell RNA sequencing, and immunofluorescence data of ESCC samples from 24 patients who received neoadjuvant treatment with PD-1 inhibitors plus paclitaxel and platinum-based chemotherapy to identify correlations with therapeutic responses.

Findings An elevation of small insertions and deletions was observed in responders. DNA mismatch repair (MMR) pathway alternations were highly frequent in patients with optimal responses and correlated with tumour infiltrating lymphocytes (TILs). Among the TILs in ESCC, dichotomous developing trajectories of B cells were identified, with one lineage differentiating towards $LMO2^+$ germinal centre B cells and another lineage differentiating towards $CD55^+$ memory B cells. While $LMO2^+$ germinal centre B cells were enriched in responding tumours, $CD55^+$ memory B cells were found to correlate with inferior responses to combination therapy, exhibiting immune-regulating features and impeding the cytotoxicity of $CD8^+$ T cells. The comprehensive evaluation of transcriptomic B cell lineage features was validated to predict responses to immunotherapy in patients with cancer.

Interpretation This comprehensive evaluation of tumour MMR pathway alternations and intra-tumoural B cell features will help to improve the selection and management of patients with ESCC to receive neoadjuvant chemoimmunotherapy.

Funding National Science Foundation of China (82373371, 82330053), Eastern Scholar Program at Shanghai Institutions of Higher Learning, National Science and Technology Major Project of China (2023YFA1800204, 2020YFC2008402), and Science and Technology Commission of Shanghai Municipality (22ZR1410700, 20ZR1410800).

Keywords: Oesophageal squamous cell carcinoma; Immunotherapy; B cells; MMR

Introduction

Immune checkpoint blockade (ICB) has shed light on new strategies to improve the survival of various solid tumours, including oesophageal squamous cell carcinoma (ESCC). As first-line therapy in patients with advanced or metastatic ESCC, anti-PD-1 monoclonal

*Corresponding author.
**Corresponding author.
***Corresponding author.
E-mail addresses: ge.di@zs-hospital.sh.cn (D. Ge), gu.jie3@zs-hospital.sh.cn (J. Gu), ronghualiu@fudan.edu.cn (R. Liu).
[e]These authors contributed equally to this work.

Research in context

Evidence before this study

No molecular or immune biomarkers are available to guide precise therapeutic strategies for patients with oesophageal squamous cell carcinoma (ESCC) yet. The development of neoadjuvant chemoimmunotherapy has shown manageable safety and great efficacy in the treatment of locally advanced ESCC. However, the expression of PD-L1 failed to predict therapeutic responses of neoadjuvant chemoimmunotherapy in ESCC, underscoring the urgent need for novel therapeutic biomarkers. Tertiary lymphoid structures, which are mainly formed by the aggregation of B cells, have now been highlighted for evoking immune responses in multiple tumours; however, the function and clinical significance of intra-tumoural B cells have yet to be determined.

Added value of this study

We demonstrate a significant association of mismatch repair pathway (MMR) alternations with treatment benefits. Dichotomous lineages of B cells developing towards $LMO2^+$ germinal centre B cells and $CD55^+$ memory B cells were identified within the tumour microenvironment of ESCC, which strongly correlated with therapeutic responses. $CD55^+$ B cells facilitate tumour growth by orchestrating immunosuppression. Additionally, a comprehensive evaluation of transcriptomic B cell lineage features can serve as an effective predictor of the response to immunotherapy.

Implications of all the available evidence

CD55 blockade may inhibit the immunosuppressive functions of B cells and contribute to the reinvigoration of anti-tumour immune responses in ESCC. The comprehensive evaluation of tumour MMR pathway alternation and intra-tumoural B cell features will improve the selection and management of patients with ESCC to receive neoadjuvant chemoimmunotherapy.

antibodies significantly prolonged progression-free survival in the KEYNOTE-590, ESCORT-1st, and ORIENT-15 trials.[1–4] The combination of anti-PD-1 monoclonal antibodies and platinum-based chemotherapy leads to superior outcomes, compared with chemotherapy alone.[5] Multiple studies have attempted to determine the feasibility and efficacy of chemoimmunotherapy in patients with potentially resectable ESCC to further expand the application. In the neoadjuvant setting, the pathologic complete response (pCR) rate of patients receiving camrelizumab plus nab-paclitaxel and carboplatin reached 39.2%.[6] However, PD-L1 expression cannot explain the heterogeneous responses of ICB in ESCC.[3,6] Besides, the predictive effect of tumour mutational burden (TMB) remains highly controversial. The TMB values were comparable between responding and non-responding groups in patients treated with Tislelizumab plus chemotherapy.[7] Nevertheless, significantly higher TMB was observed in tumours with pCR comparing to tumours without pCR from patients treated with camrelizumab plus chemotherapy.[6] The cellular and molecular mechanisms of response are fundamental knowledge barriers in expanding the proportion of patients with ESCC who benefit from ICB.

Studies have illustrated that mutation-associated neoantigens (MANAs) derived from tumour somatic mutations have divergent immunogenicity and may promote distinct adaptive immune responses after recognised by immune cells. In adaptive immune responses, tumour-infiltrating B cells play key roles in presenting antigens to T cells, stimulating $CD4^+$ T cells,[8] and organizing tertiary lymphoid structures (TLSs), which positively correlate with immunotherapy efficacy.[9,10] However, immunosuppressive signaling within tumour ecosystems can lead to reprogramming of lymphocytes, including B cells, resulting in resistance to immunotherapy. Our work aimed to characterize the genomic and immune features correlated with heterogeneous responses to neoadjuvant PD-1 inhibitors plus paclitaxel and platinum-based chemotherapy. Consequently, we discovered the comprehensive evaluation of tumour MMR pathway alternations and intratumoural B cell features will provide a more accurate prediction for patients with ESCC who will respond to therapy.

Methods

Patient population

Between February 2021 and January 2022, 24 patients with histologically confirmed locally advanced ESCC were enrolled in this study. After pretreatment biopsy, all patients received preoperative anti-PD-1 therapy plus paclitaxel-platinum-based chemotherapy for 2–4 cycles and then underwent R0 resection surgery (Figure S1 and Table S1). Additionally, we collected five surgical tumour samples from patients with untreated ESCC and performed flow cytometry to validate the infiltration and phenotypes of B cell subsets.

For therapy response evaluation, we applied the Mandard tumour regression grade (TRG) system as a surrogate endpoint, which is associated with mortality in oesophageal cancer after neoadjuvant therapies.[11] Patients with TRG grades 1–2 were regarded as responders and patients with TRG grades 3–5 were regarded as non-responders. This neoadjuvant treatment cohort included six females (25%) and 18 males (75%), which is basically concordant with the reported sex disparities in ESCC incidence.[12] Sex of participants was determined by biological secondary sex characteristics. All patients provided written informed consents

and the study was approved by the Ethics Committee of Zhongshan Hospital, Fudan University (B2021-129).

Whole-exome sequencing (WES) and somatic variant detection

DNA was extracted from formalin-fixed paraffin-embedded (FFPE) sections using Nucleic Acid Extraction Kits and Concert-HF-48 Nucleic Acid Purifier (Concertbio). All FFPE specimens from 23 patients were sequenced within six months after sampling. WES libraries were constructed by NadPrep DNA Library Preparation Kit (Nanodigmbio) from 500 ng FFPE-DNA. Library yields were controlled between 500 and 1000 ng. All WES libraries were processed by single-tube capture hybridization, following the Nanodigmbio Hybridization capture protocol, and target capture with NEXome Plus Panel v1.0 (Nanodigmbio) was performed overnight. Streptavidin M270 beads were used to isolate hybridized targets. WES libraries were then sequenced by 150bp paired-end runs at a sequencing depth of 300–500x using a DNBSEQ-T7RS Sequencer (MGI Tech Co, Shenzhen China). The frequencies of C > T transitions were comparable between our pre-treatment samples and those reported in The Cancer Genome Atlas (TCGA)-ESCC cohort. For bioinformatic filtering, we set the variant allele frequency threshold to 5%. Quality control data of WES are provided in Table S2.

Gapped alignment of the reads was performed with the Burrows-Wheeler-Aligner-0.7.17-r1194 software and the Genomic Variant Caller algorithm (GVC; Genome Wisdom Inc) utility was used to detect somatic variations. GVC employs a machine learning model to calculate the probability of single nucleotide variants (SNVs), small insertions and deletions (indels), and copy number variations (CNVs) for different genotypes of tumour and normal control samples. For the calling of structural variation, GVC extracts the reads from the BAM file related to fusion candidates and also extracts the feature information near the fusion breakpoints.

Signature analysis, human leucocyte antigen (HLA) typing, and neoantigen prediction

Mutational signature analysis, with reference to COSMIC cancer signatures,[13] was performed using deconstructSigs (1.6.0), which selects combinations of known mutational signatures that account for the observed mutational profile in each sample. Mutational signatures were represented by the following terms: MMRD (SBS6 and SBS15), age (SBS1 and SBS5), APOBEC (SBS2 and SBS13), smoking (SBS4), UV (SBS7), POLE (SBS10a and -b), colibactin exposure (SBS88), aristolochic acid exposure (SBS22), and aflatoxin exposure (SBS24).

HLA class I types were determined for each tumour and matched normal sample by Polysolver tool (4.0) from the WES with default parameters. HLA loss of heterozygosity (LOH) was defined as LOH over the HLA class I locus (HLA-A/B/C). The LOHHLA tool was used to determine LOH over the HLA class I locus. Less than 0.5 copy number statistically significant HLA alleles were thought to be experiencing loss of heterozygosity. Neoepitopes (9-mers) containing nonsynonymous SNV and indel mutations were predicted by NetMHCpan v4.1. Candidate neoantigens were selected by the following criteria: (1) class I HLA-binding affinity of neoepitope is less than 500 nM and (2) the rank of tumour neoepitope is less than 0.5%.

Single-cell RNA-sequencing (scRNA-seq) and data analysis

Ten freshly resected EESC surgical specimens were collected for scRNA-seq. After being dissociated into single cells, fresh ESCC samples were stained with anti-CD45 and fluorescently conjugated antibodies. The antibodies used in this study are listed in Table S3. $CD45^+$ dye^- live immune cells were purified by the Melody fluorescence-activated cell sorter (FACS) and the BD Rhapsody system was applied to capture single cells. Whole-transcriptome libraries were prepared using the BD Rhapsody single-cell whole-transcriptome amplification workflow. An Illumina sequencer (Illumina, San Diego, CA, USA) was used for sequencing on a 150-bp paired-end run. UMI-tools were used to identify the cell barcode whitelist. The UMI-based clean data were mapped to the human reference genome (Ensemble V.91) using the STAR algorithm. Raw data were processed using fastp to filter adaptor sequences and remove low-quality reads. Cells with a mitochondrial content higher than 30% were regressed out from further downstream analysis. After filtering cells with high expression of mitochondrial DNA and ribosomal RNA, we obtained 32,429 $CD45^+$ immune cells. Through cell type annotation by SingleR (1.8.1), we clustered the major immune cell subtypes, which included 7460 follicular B cells, 2383 germinal centre (GC) B cells, 476 plasma cells, 1473 myeloid cells, 1941 NK cells, 8733 $CD4^+$ T cells and 9963 $CD8^+$ T cells. For the integration of scRNA-seq data from each patient, the Harmony algorithm (0.1.2) was used to batch correct the samples (patient was used as the batch variable). Pseudo-time trajectory analysis was performed by Slingshot (3.16), comparison of cell density in lineages was performed by condiments (1.6.0), and intercellular communication was analysed with CellPhoneDB (3.0.0).

Co-culture of B- and T-cells

Human cells were acquired from patients with ESCC for FACS. $CD45^+CD3^+CD4^+$ T cells and $CD45^+CD3^+CD8^+$ T cells were sorted on a BD FACsAria flow cytometer based on CD45, CD3, CD4, and CD8 surface expression phenotypes. $CD45^+CD19^+CD55^+$ B cells and $CD45^+CD19^+CD55^-$ B cells were sorted on the BD FACsAria flow cytometer based on $CD45^+$, $CD19^+$, and $CD55^{+/-}$ surface expression phenotypes. Purified B-cell

(2×10^4 cells/well) and T-cell (2×10^5 cells/well) subsets from the same patient were plated in a 48-well U-bottom plate and co-cultured for 48 h with anti-CD3 (2 mg/mL), anti-CD28 (10 mg/mL), interleukin (IL)-2 (0.2 mg/mL), anti-IgM (2 mg/mL), and lipopolysaccharide (10 mg/mL). Flow cytometry was used to analyse the composition of T cells.

Mice

Ten male NOD-SCID mice (RRID: BCBC_1262) of ten weeks-old were used in this study. The mice were housed at temperatures of 18–23 °C with 40–60% humidity under specific pathogen-free conditions and fed a normal diet. Environmental enrichment, including nesting and houses, was provided to promote welfare. No animal was excluded in analysis and no unexpected adverse events occurred. Animal experiments were conducted in compliance with protocols approved by Zhongshan Hospital, Fudan University, with permission granted under approval number SYXK 2021-0022.

Cell lines

The ESCC cell line EC-109 (RRID: CVCL_6898) was obtained from the Institute of Biochemistry and Cell Biology of the Chinese Academy of Science (TCHu 69, Shanghai, China), which was authenticated using short tandem repeat profiling. The cell line was used in the sixth month after receipt. EC109 cells were cultured in Dulbecco's modified Eagle medium containing 10% foetal bovine serum. The cells were grown at 37 °C in a 5% CO_2 atmosphere.

Adoptive transfer

To conduct the in vivo cell transfer experiment, we collected lymphocytes from surgical ESCC specimens from five patients and isolated $CD8^+$ T cells using CD8 Microbeads (STEMCELL). In vitro co-culture of the isolated $CD8^+$ T cells and EC109 cells for 8 h was conducted first to verify that the $CD8^+$ T cells can recognise and kill EC109 tumour cells. Among five patients, the one whose $CD8^+$ T cells expressed highest levels of CD107a after co-culture was selected as the lymphocyte donor for the in vivo cell transfer experiment. HLA I compatibility was examined by GENDX SBTexcellerator to support $CD8^+$ T cells from the donor may recognise EC109 cells in a MHC-I dependent manner.

Previous studies have reported the adoptive transfer of lymphocytes to male tumor-bearing mice.[14,15] Only male mice were used to avoid the different efficacy of tumor transplantation and adoptive transfer caused by the discrepancy of sex. The ten NOD-SCID mice of ten weeks-old were randomly divided into two groups for different adoptive transference (five mice per group). The FACS-purified $CD55^+$ B cells (4×10^5 cells), $CD55^-$ B cells (4×10^5 cells), and $CD3^+$ T cells (1×10^6 cells) from the tumour of the donor were transferred into each NOD-SCID mouse from the two groups via intravenous injection. After 48 h, the subcutaneous ESCC model was established with injection of EC109 cells (3×10^5 cells) to each mouse. The same adoptive transfer protocol was repeated for each mouse 17 days after construction of the subcutaneous ESCC model. The mice were sacrificed at the end point of the study and subcutaneous tumours were excised and processed for further analyses. All procedures were conducted by researchers in accordance with the Guide for the Care and Use of Laboratory Animals.

Bulk RNA sequencing data source and processing

Patient characteristics of the TCGA-ESCC cohort were retrieved from http://www.cbioportal.org/study. The ICB cohort was composed of patients from the GO29293 cohort,[16,17] which includes 451 patients with solid tumours who received atezolizumab. The gene signatures of the $CD55^+$ memory B (Bm) cells and the $LMO2^+$ GCB cells were constructed by top expressed genes of the Bm_CD55 and GCB_LMO2 subsets from the scRNA-seq data. The component of gene signatures and mutational pathways used in this study are listed in Table S4. GSVA package (1.48) was used to calculate the ssGSEA score for each gene signature for every sample in the TCGA-ESCC and ICB cohorts.

A support vector machine (SVM) classifier with linear kernels was used to verify the robustness of the K-means clustered subgroups. We used leave-one-out cross-validation to predict K-means clustered subgroup membership.[18] To avoid overfitting, the regularization parameter was set to 1 for each binary classification problem, and the assigned vector of length was fixed to a uniform vector under the assumption that each binary classification problem is equally important. The performance of the multiclass classifier was evaluated through the construction of receiver operating characteristic curves and measurement of the area under the curve (AUC); the mean AUC was 0.972 for the categorization, supporting the stability of K-means clustering.

Statistical analysis

The continuous variables were evaluated between two conditions by the Mann–Whitney *U* test and the categorical variables were evaluated between two conditions by the Chi-squared test or Fisher exact test. Correlation was carried out with Spearman's rank test. Data are presented as box plots, including the median (centre line) with 25th and 75th percentiles (box limits) and standard deviation (error bars). Kaplan–Meier curves were used for overall survival (OS) and progression-free survival (PFS) analyses, and the log-rank test was used to compare survival between two groups. Univariate and multivariate logistic regression was used to analyse variables and dichotomous status and to identify potential confounders and bias in the study. Univariate and multivariate analyses were performed by Cox proportional-hazards regression with hazard ratios and

95% confidence intervals. Specific statistical tests corresponding to each analysis are detailed in the figure legends. The medians were defined as cut-offs to categorize samples according to high and low values of continuous variables. The statistical analyses were performed using R (3.4) and IBM SPSS Statistics V.26.0 (SPSS, Chicago, IL, USA). A two-sided P value <0.05 was considered statistically significant.

Role of funders
The funders were not involved in the study design, data collection, data analysis, interpretation or writing of the manuscript.

Results

Exonic mutational landscapes of ESCC associated with response to therapy

To dissect genomic and immune profiles and identify the determinants of therapeutic efficacy in ESCC, we leveraged WES, scRNA-seq, and immunohistochemistry/multiplex immunofluorescence (mIF) data in ESCC samples from 24 patients who received neoadjuvant PD-1 inhibitors plus paclitaxel-platinum-based chemotherapy and subsequent surgeries (Fig. 1a and Figure S1). The responses to treatment were assessed via computed tomography and underwent pathological review (Fig. 1b). TRG 1 was achieved in four patients, TRG 2 in eight patients, and TRG 3–5 in 12 patients (Fig. 1c). Among the 23 pretreatment tissues analysed by WES, the TMB was higher in responders than in non-responders (5.52/Mb vs 2.76/Mb; P = 0.038, Mann–Whitney *U* test; Fig. 1d). However, pre-treatment TMB was not a significant predictor of the therapy response (Table S5). We then found that responding samples carried significantly higher raw counts of indels, rather than SNVs, than samples from non-responders (71 vs 32; P = 0.005, Mann–Whitney *U* test). The prediction values of pre-treatment SNVs, indels and CNVs based on raw counts suggested that pre-treatment indels showed the highest AUC value (Figure S2a). Collectively, these results indicated that the pre-treatment indel burden predicts the response to neoadjuvant chemoimmunotherapy in patients with ESCC, independent of potentially confounding factors (Table S5), which is in line with recent studies.[19]

Interestingly, we observed that *FAT1* mutations were completely preserved in non-responders after treatment (Fig. 1e). In addition, patient S4, who harboured a considerable TMB but no mutations in the NOTCH pathway before treatment, exhibited limited benefits from neoadjuvant chemoimmunotherapy, implicating that NOTCH alternations may enhance chemoimmunotherapy responsiveness.[20] *POLE* (1/11 vs 0/12; P = 0.478, Fisher's exact test), *MLH1* (2/11 vs 0/12; P = 0.217, Fisher's exact test), and *OGG1* (2/11 vs 0/12; P = 0.217, Fisher's exact test) mutations were exclusively identified in responders before treatment, implicating that deficient DNA damage repair (DDR) might be associated to therapeutic responses in ESCC. These results were enlightening but inconclusive. Moreover, comparisons of pathway alternation frequencies between responders and non-responders in pre-treatment samples revealed increased alternations in the PI3K, BER, MMR, and FA pathways[21,22] in responders (Fig. 1f). In this analysis, a patient was considered to carry a pathway alternation if a mutation in a gene in a pathway was found in any of the preoperative tissues. In the mutational signature analysis, MMR deficiency signatures were significantly preponderated in patients with TRG1 (Fig. 1g and Figure S2b).

To further investigate the relationship between DDR pathways and therapeutic efficacy, we designated tumours with alternations in the MMR, BER, or FA pathways as tumours with DDR alternation. Univariable logistic analysis showed that the integrated pre-treatment DDR alternations showed strong potency in predicting the therapeutic responsiveness (Fig. 2a). In pre-treatment samples, tumours with DDR alternations possessed higher TMB and SNV levels, and the disparity was exacerbated when comparing the number of indels between two groups (Fig. 2b).

Intriguingly, we noted that some patients with relatively high pre-treatment TMB or DDR alternations still exhibited suboptimal clinical benefits. Since defects in antigen presentation may obstruct neoantigen recognition and activation of immune responses, we next inspected the LOH in HLA and alterations of genes of the antigen-presenting machinery. While defects in the antigen-presenting machinery exhibited no difference between responders and non-responders (Fig. 2c), HLA LOH was observed only in non-responders both before and after treatments (Fig. 2c and d). We further discovered that all patients with pre-treatment DDR alternations and intact HLA responded to chemoimmunotherapy (Fig. 2d). Therefore, it is inferred that pre-treatment DDR alternations may only facilitate an immune response when the HLA remains intact.

To assess the immunological mechanisms driving distinct therapeutic responses among patients with varied DDR status, we examined corroborated genomic and immune data[23] from the ESCC-TCGA cohort. Significant elevation of immune cells, including total lymphocytes, $CD8^+$ T cells, follicular helper T cells, and naïve B cells, and decreased memory B cells were observed in patients with MMR alternations compared to patients with other DDR alternations or no DDR alternations (Fig. 2e), implying an upsurge in the adaptive immune response. Moreover, the number of mutated MMR genes in pre-treatment specimens correlated negatively with the percentage of residual viable tumour cells after treatment (Fig. 2f).

To further explore the mechanism underlying the association between MMR alternations and therapeutic

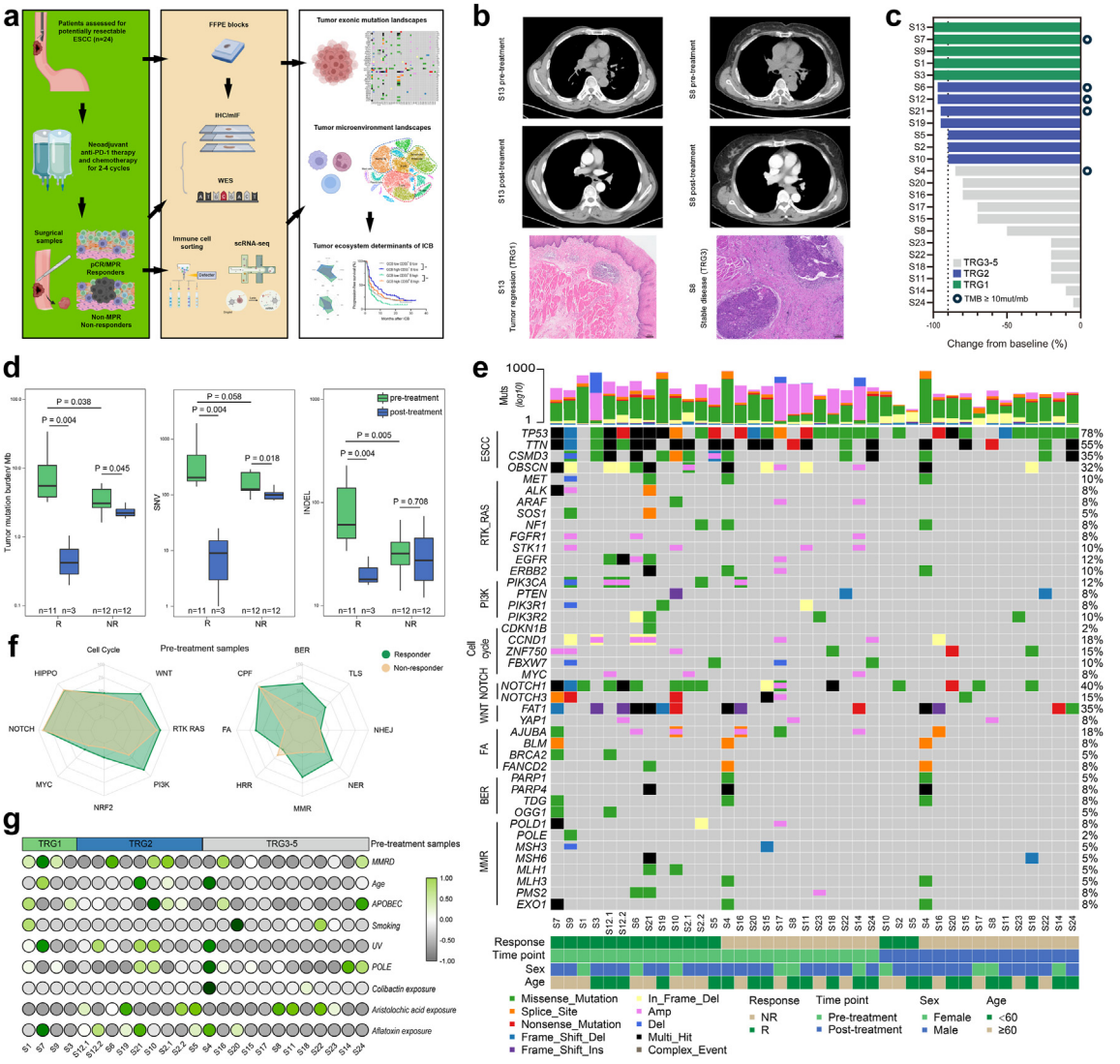

Fig. 1: **Exonic mutational landscapes of ESCC associating to therapeutic responses.** **(a)** The schematic of the study workflow summarizing the analysis of genomic and immune profiling in this study. **(b)** Representative computed tomography images and H&E images obtained during patient treatment. Scale bar, 100 μm. **(c)** Bar chart of the pathological response for each patient included for analysis. **(d)** Box plot comparing TMB, SNV and indels between responders and non-responders before and after treatment (Mann–Whitney *U* test). **(e)** Landscape of genomic alterations in pre-treatment and post-treatment samples from the patients with ESCC matched according to pathological responses. **(f)** Radar chart displaying the frequencies of pathway alternations in pre-treatment samples from responders (n = 11) and non-responders (n = 12). **(g)** Heatmap of mutational signatures in pre-treatment samples from patients with ESCC matched according to pathological responses. The number of samples and P values are indicated directly in the figure. Error bars in bar plots represent the standard deviation.

responses, we applied neoantigen binding affinity prediction to determine whether MMR alternations were associated with high-affinity mutation-associated neoantigens (MANAs). Although the pre-treatment counts of overall MANAs and indel-derived MANAs failed to distinguish the difference in therapeutic responses, the proportion of patients who carried pre-treatment indel-derived MANAs was higher in responders than in the non-responders (Fig. 2g and Figure S2b), suggesting the superior immunogenicity of the indel-derived neoantigens. Additionally, the proportion of tumours carrying pre-treatment indel-derived neoantigens was higher in cases of ESCC with MMR alternations than tumours without MMR alternations (Fig. 2g). The Sankey diagram (Fig. 2h) demonstrates the relationship between dynamic genomic profiling and therapeutic responses. The

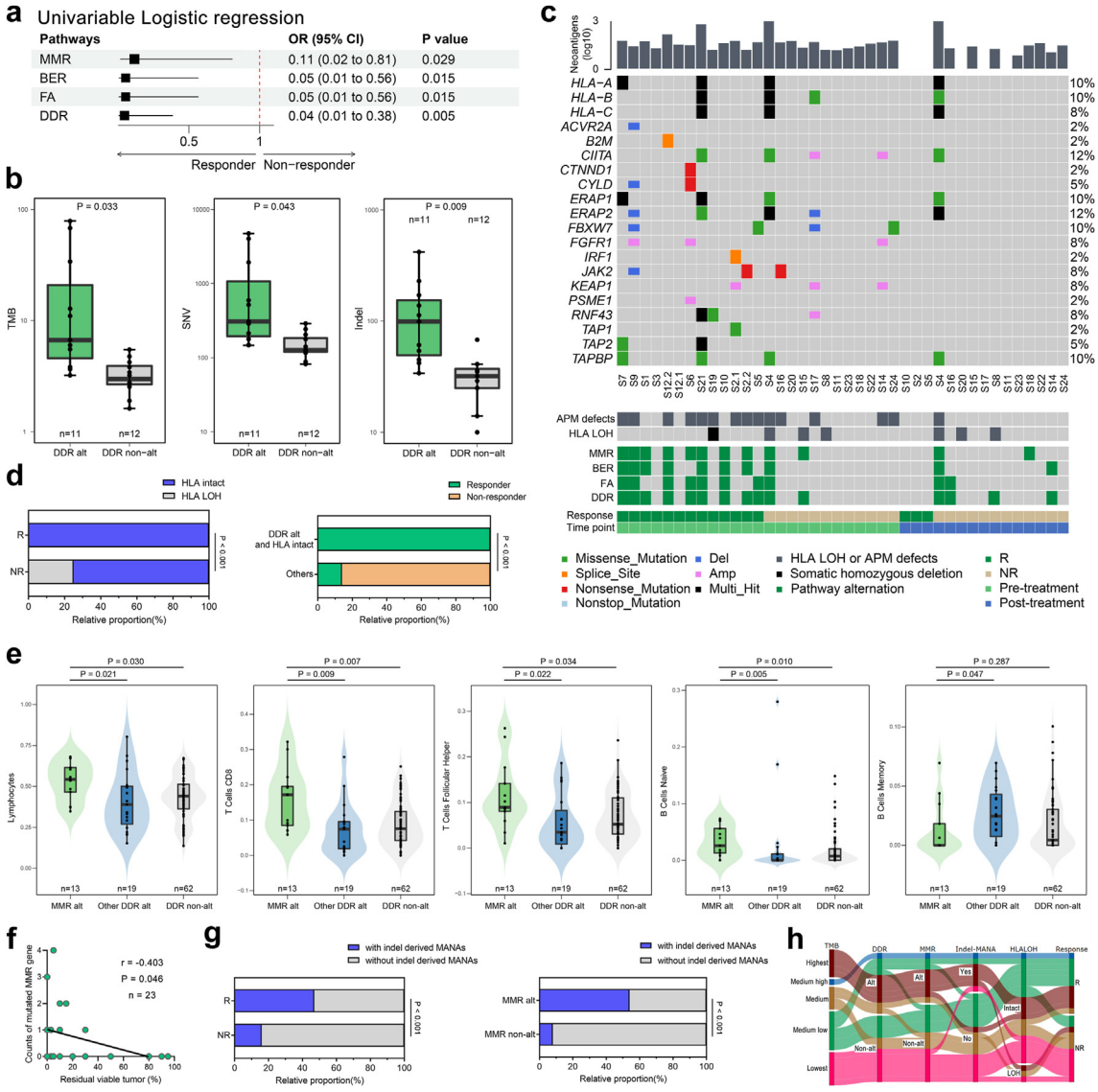

Fig. 2: **Association of damaged DNA repair pathways with therapeutic responses. (a)** Forest plot representing the odd ratios with error bars corresponding to 95% CI bounds determined by the univariable Logistic regression model. **(b)** Box plot comparing pre-treatment TMB, SNV and indels between patients with and without DNA damage repair (DDR) alterations (Mann–Whitney *U* test). **(c)** Landscape of antigen presenting gene alterations and HLA LOH status in pre-treatment and post-treatment samples from the patients with ESCC matched according to pathological responses. **(d)** Proportions of pre-treatment HLA LOH events in responders (n = 11) vs non-responders (n = 12) (0% vs 36.6%, Chi-square P < 0.001) (left); proportions of responders in patients with pre-treatment DDR alt and HLA intact (n = 9) vs others (n = 14) (100% vs 15.4%, Chi-square P < 0.001) (right). **(e)** Violin plot comparing lymphocytes, $CD8^+$ T cells, T cell follicular helpers, naïve B cells and memory B cells according to DDR status (Mann–Whitney *U* test). (**f**) Correlation between numbers of treatment mutated MMR genes and residue viable tumour (%) (Spearman's rank test). (**g**) Proportions of patients with pre-treatment indel derived MANAs in responders (n = 11) vs non-responders (n = 12) (47% vs 16%, Chi-square P < 0.001) (left) and in MMR alt (n = 9) vs MMR non-alt (n = 14) (54% vs 8%, Chi-square P < 0.001) (right). (**h**) Sankey diagram depicting the flow of therapeutic responses across genomic profiling. APM, antigen-presenting machinery. HLA, human leukocyte antigen. LOH, loss of heterozygosity. The number of samples and P values are presented in the figure. Error bars in bar plots represent the standard deviation.

predictive effect of pre-treatment MMR alternations on therapeutic responses appeared to be consistent when adjusting for potential confounders of ESCC (Table S5).

In summary, our results indicate that DDR alternations, especially MMR alternations, might increase the indel-derived MANA burdens that activate immune

responses and consequently influence the clinical outcomes of neoadjuvant chemoimmunotherapy.

Immune infiltration heterogeneity of ESCC with distinct therapeutic responsiveness

Heterogeneity of the tumour microenvironment (TME) strongly interacts with genomic alterations within tumour cells and determines the response to chemoimmunotherapy. Both pre-treatment $CD8^+$ cells and PD-L1 expression scores on FFPE slides failed to distinguish responders from non-responders (Figure S3a and b). To further investigate the immunological determinants, 10 tumour samples were collected from surgery after neoadjuvant treatment and analysed using scRNA-seq for panoramic illustration of the TME of patients with distinct susceptibility to treatment. After quality control, eight main immune cell clusters were formed: $CD4^+$ T cells, $CD8^+$ T cells, NK cells, follicular B cells, germinal centre B (GCB) cells, plasma cells, and myeloid cells (Fig. 3a). Interestingly, *PDCD1* and *CD274* expression levels were elevated in non-responding tumours after treatment, especially in GCB cells and $CD4^+$ T cells, respectively (Fig. 3b). We then examined the relative frequencies of immune cells in patients with varied MMR status and therapeutic sensitivities. Enriched follicular B cells and down-regulated $CD8^+$ T cells were observed in patients with MMR alternations. In addition, follicular B cells increased in responsive tumours, whereas $CD4^+$ T cells mainly infiltrated non-responsive tumours (Fig. 3c).

Since we identified differentially enriched lymphocyte clusters in patients with distinct therapeutic responses, we further re-clustered $CD8^+$ T cells, $CD4^+$ T cells, and B cells to provide insights into the specific immune populations that may drive therapeutic responses in ESCC (Fig. 3d). Six $CD8^+$ T cell clusters were categorized (Figure S4a and b). A tendency of upregulated central memory $CD8^+$ T cells and effector $CD8^+$ T cell was observed in responders (Figure S4c). For $CD4^+$ T cells, we identified seven canonical $CD4^+$ T cell clusters and two Treg clusters (Fig. 3e and Figure S4d). Compared with responders, non-responders showed infiltration of lower proportions of central memory $CD4^+$ T cells, but higher proportions of IL-26^+ $CD4^+$ T cells and Tregs (Fig. 3f), which is in line with previous reports of immune modulation caused by Tregs and $CD4^+$ T cell-derived IL-26.[24,25]

When sub-clustering B cells, we detected seven clusters and investigated their association with therapeutic susceptibility (Fig. 3g). The Bn_YBX3 cluster was characterized by highly expressed naïve markers *IGHM* and *IGHD*. Two GCB cell subsets were detected through the specific expression of *POU2AF1* and *LMO2*, and a preGC subset was distinguished by *PARVB* and *FCRL3* expression. Moreover, the other four clusters displayed a transcriptomic profile that resembles that of memory B cells by expressing P2RY10 and *VIM* (Figure S4e and f). We further investigated the transcriptomic profile of the B cell clusters. By identifying the features of two GCB cell subsets, GCB_STMN1 was found to express high levels of cell cycle genes, including *MKI67* and *TOP2A*, consistent with a proliferating B cell population in the GC.[9,26] The other GCB cell cluster exhibited elevated expression of *LMO2*. Memory B cells were transcriptomically heterogeneous, among which the Bm_CD55 subset designated by *CD55* expression expressed the highest level of activation markers (Figure S4f). We observed that GCB_LMO2 exhibited high relative abundance in patients harbouring MMR alternations. Likewise, the infiltration of GCB_LMO2 cell tended to increase in responsive tumours, while that of Bm_CD55 cells decreased (Fig. 3h and Figure S4g and h). These findings emphasise the importance of B cell heterogeneity in shaping the clinical outcomes of chemoimmunotherapy in ESCC.

Dichotomous developing trajectories of B cells in ESCC

To gain insight into the mechanisms underlying B cell heterogeneity in the TME with distinct therapeutic responses, we identified differentially expressed genes in B cells between responding and non-responding samples (Figure S5a and Table S6). Among these, the levels of *IGHM* and antigen presentation genes (*HLA-DMB* and *CIITA*) were increased in responders, while the expression of *IGHA1*, *DDX21*, and *CD55* was significantly upregulated in non-responders (Fig. 4a). Next, we established GSVA scores of canonical B cell signatures to identify enriched characteristics. Notably, signatures of B cell immaturity, GC initiation, and the tertiary lymphoid structure (TLS) increased in responding tumours.

To better understand the dynamic changes in B cells in the setting of chemoimmunotherapy, we applied Slingshot to reconstruct the pseudotime trajectories. Based on the UMAP representation, Bn_YBX3 was set as the starting point, and the end point was inferred via pseudotime ordering. Intriguingly, two divergent lineages were established: a GC entry lineage extended to GCB cell subsets and a Bm activation lineage differentiated towards $CD55^+$ memory B cells (Fig. 4b and Figure S5b). Differentially expressed gene analysis showed that *BCL6* and *LMO2* expression increased with pseudotime in the GC entry lineage, while TNFRSF13B and *VIM* were upregulated in the Bm activation lineage (Fig. 4c and Table S7). We also found progressive increases in MHC II and B cell activation signatures according to pseudotime in GC entry lineage and Bm activation lineage, respectively (Fig. 4c). This finding is in line with a previous report showing that the B cell activation feature increased in antigen-experienced memory B cells and diminished in GCB cells.[27]

Determination of the developmental status analysis of B cells showed that B cells from samples of responders were located in the early portion of both

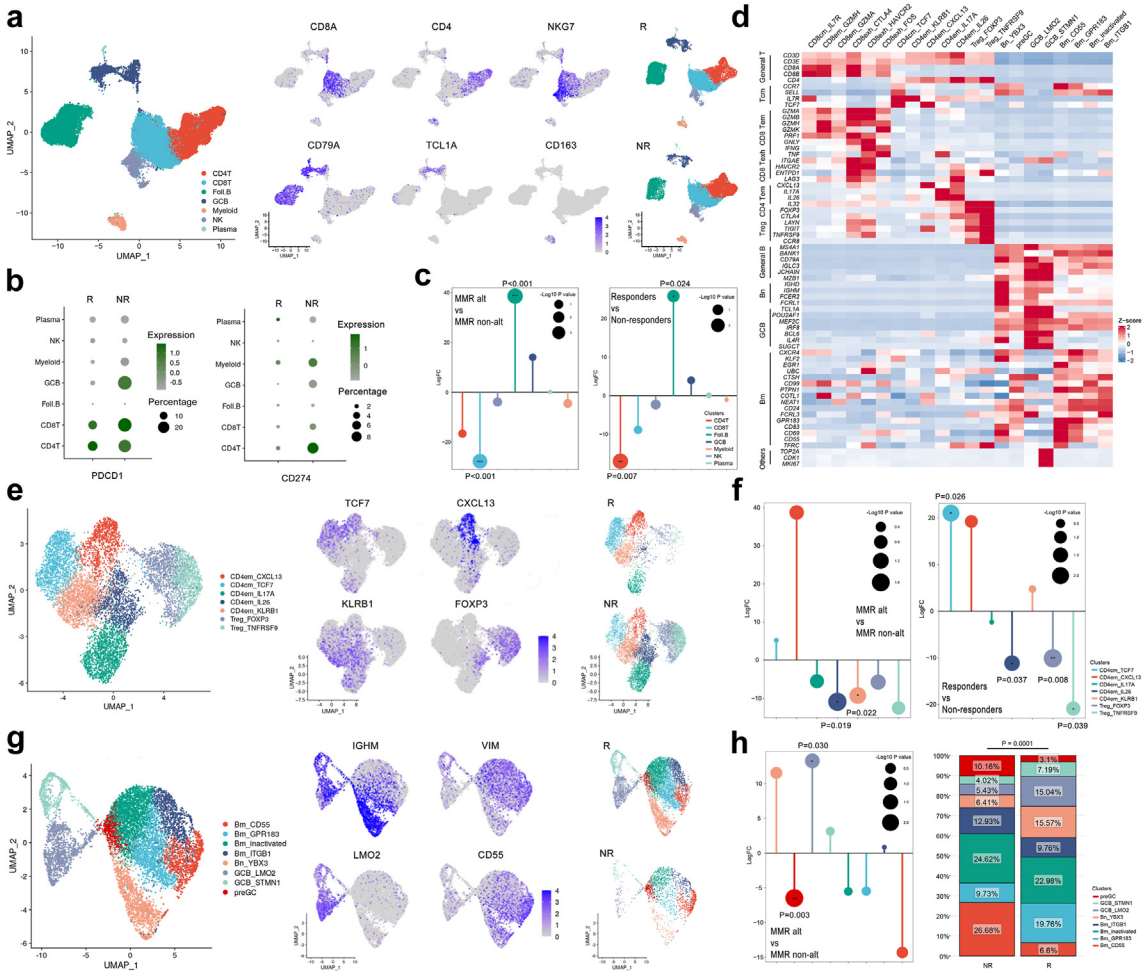

Fig. 3: **Immune infiltration heterogeneity of ESCC with distinct therapeutic responses. (a)** UMAP plot showing clustering for immune cells from 10 patients with ESCC (left), expression of selected genes (middle) and distribution according to different therapeutic responses (right). **(b)** Dot plot showing the expression of *PDCD1* and *CD274* in immune cell clusters from responders and non-responders. **(c)** Lollipop chart showing difference of proportions of immune cell clusters in patients with different MMR status (left) and therapeutic responses (right) (scales of circles indicate the –log P value; Student's t test). **(d)** Expression heatmap of signature genes in distinct lymphocyte clusters. **(e)** UMAP plot showing the subclustering for $CD4^+$ T cells from 10 patients with ESCC (left), expression of selected genes (middle) and distribution in different therapeutic responses (right). **(f)** Lollipop chart showing differences of proportions of $CD4^+$ T cell subclusters from patients with different MMR status (left) and therapeutic responses (right) (scales of circles indicate the –log P value; Student's t test). **(g)** UMAP plot showing the subclustering for B cells from 10 patients with ESCC (left), expression of selected genes (middle) and distribution according to different therapeutic responses (right). **(h)** Lollipop and column chart showing difference of proportions of B cell subclusters from patients with different MMR status (scales of circles indicate the –log P value; Student's t test; left) and therapeutic responses (Chi-square test; right). P values are indicated in the figure.

trajectories and in the late position of the GC entry lineage, whereas B cells from samples of non-responders were located in the intermediate portion of the GC entry lineage and in the late stage of the Bm activation lineage (Fig. 4d). The skew towards GCB cells in responders and that towards activated memory B cells in non-responders is concordant with the aforementioned differential infiltration of the GCB cell subsets and Bm_CD55 subset. Significant activation of pathways involving cytokine binding and inflammatory response was observed in GC entry lineage, along with down-regulation of immunoglobulin production and B cell activation pathways (Fig. 4e). In summary, our data supports two linear trajectories associated with distinct B cell phenotypes, with GCB cells more frequently found at the end of the GC entry lineage, and activated memory B cells located later in the pseudotime trajectory of the Bm activation lineage.

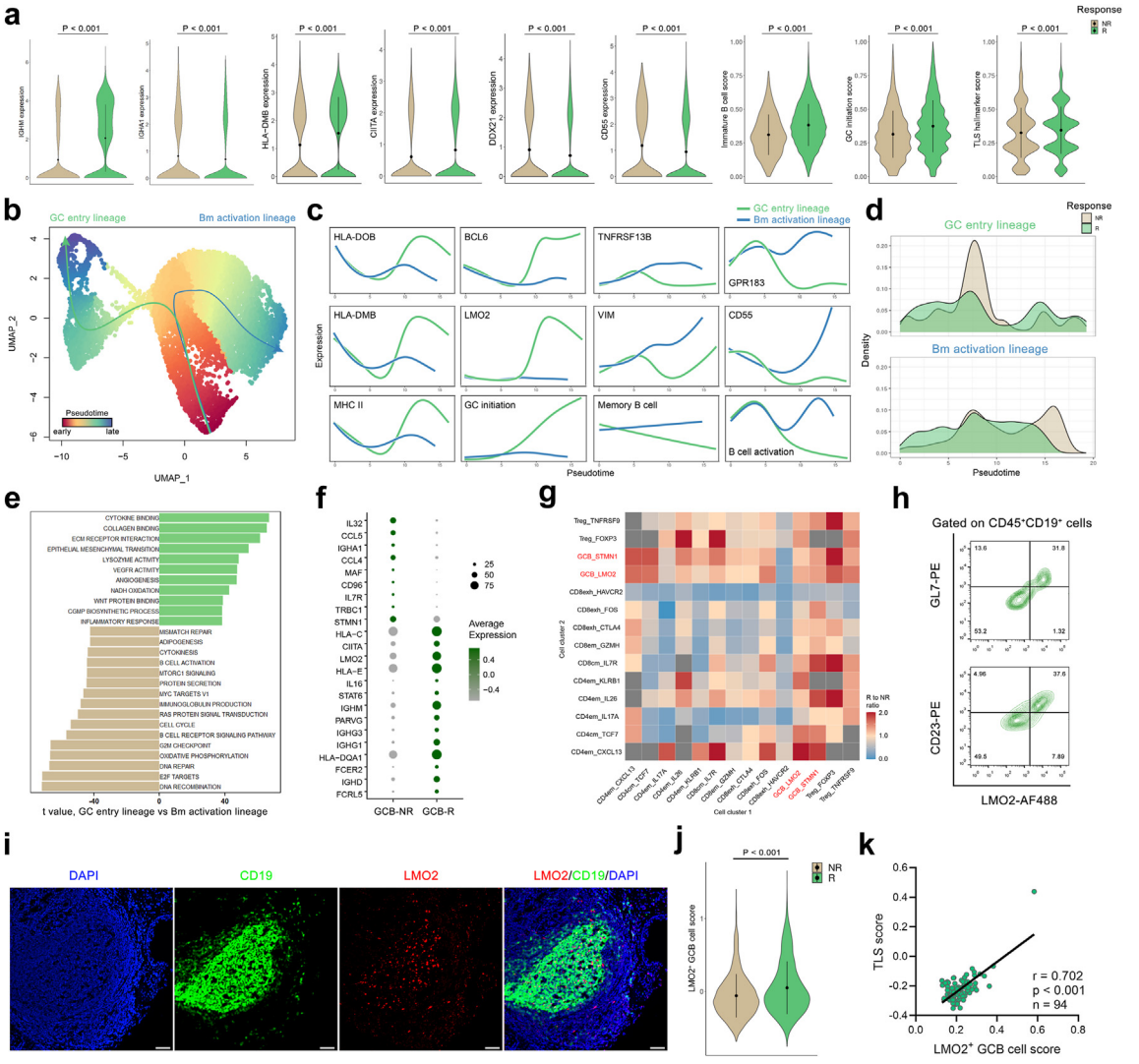

Fig. 4: **Dichotomous B cell lineages correlate with therapeutic responses. (a)** Violin plot showing the expression levels of genes and signatures in B cells from responders and non-responders (Mann–Whitney *U* test). **(b)** Pseudotime trajectories for B cells based on Slingshot, highlighting two lineages; the colour is annotated for pseudotime. **(c)** Expression of genes and signatures along pseudotime within two B cell lineages. **(d)** Histogram showing distribution of B cells from responders and non-responders according to pseudotime for the two lineages. **(e)** Bar plot showing differential pathways enriched in GCB entry lineage and Bm activation lineage by GSVA; the *t*-value is determined by a two-sided unpaired limma-moderated *t* test. **(f)** Differential expressed genes in GCB cells from responders and non-responders. **(g)** Heatmap showing the ratio of the number of significant interacting pairs between GCB cells and T cell clusters in responders and that in non-responders, identified by CellphoneDB. **(h)** Representative flow cytometric plots of the expression of GL7 and CD23 on LMO2$^+$ B cells. **(i)** Representative immunofluorescence staining of a TLS for CD19 (green) and LMO2 (red) in ESCC samples. DAPI staining is shown in blue. Scale bar, 30 μm. **(j)** Violin plot showing comparison of LMO2$^+$ GCB cell signature between B cells from responders and non-responders (Mann–Whitney *U* test). **(k)** Correlation between the TLS signature and LMO2$^+$ GCB cell signature in TCGA-ESCC (Spearman's rank test). P values are indicated in the figure. Error bars in bar plots represent the standard deviation.

GCB cells are enriched in ESCC benefitting from ICB

Next, we sought to investigate the phenotype of B cells in ESCC. Since responsive patients exhibited higher GCB cell levels than patients resistant to the chemo-immunotherapy, we investigated the function of GCB cells within the TME. Discrete markers were then identified in GCB cells from responders and non-responders (Figure S5c and Table S8). The expression of antigen-presenting genes, especially MHC II (*HLA-DQA1*), and immunoglobin (*IGHM* and *IGHD*) genes was upregulated in GCB cells from responders (Fig. 4f). To infer the mechanisms by which GCB cells promote

treatment responsiveness in the TME, we identified significant ligand–receptor pairs between GCB cells and various T cell subsets in responders and non-responders. An increased number of interacting pairs between GCB cells and T cells was observed in responders, especially between the GCB_LMO2 and CD4em_CXCL13 clusters (Fig. 4g).

Given that LMO2 was found to be preferentially expressed in GCB cells from responding tumours, we sought to define LMO2 as a specific marker for GCB cells. By performing flow cytometry with fresh ESCC samples, we discerned the co-expression of LMO2 with the conventional GCB cell markers GL-7 and CD23 (Fig. 4h), concordant with previous findings.[28] Recent studies indicated a significant benefit of the TLS to ICB in various tumours,[10,29,30] and GC structures have been revealed as key compartments in TLS formation.[31] Therefore, we further investigated the distribution of the LMO2$^+$ GCB cells. Through mIF, LMO2$^+$ B cells were identified in the TLS (Fig. 4i). Moreover, the gene signature of GCB_LMO2 cluster was constructed, which showed a dominance of B cells from responders (Fig. 4j). Transcriptomic expression of the LMO2$^+$ GCB cell score was also highly correlated with that of the TLS signature (Fig. 4k). Therefore, our data illustrated that LMO2$^+$ GCB cells were dispersed in the TLS in ESCC, promoting an anti-tumour immune response and possibly contributing to improved chemo-immunotherapy responsiveness.

Immunosuppressive characteristics of CD55$^+$ B cells in ESCC

The analyses described above revealed that CD55$^+$ B cells may play a central role in mitigating therapeutic responses. Thus, we generated a gene set of CD55$^+$ Bm cells that were increased among the B cells from non-responders (Fig. 5a). From post-treatment ESCC tissue slides, we discovered that CD55$^+$ B cells were mainly located outside the TLS and infiltrated the tumour stroma (Fig. 5b). To further illustrate CD55$^+$ B cell phenotypes, we detected differentially expressed genes and pathways between CD55$^+$ B cells and CD55$^-$ B cells (Table S9). Of note, we found that the expression of *LMO2* was significantly downregulated with the increase of *CD55* expression (Fig. 5c), which underlines the notion that *CD55* expression disturbs affinity maturation and GC initiation.[32] Moreover, GSVA scoring of B cells indicated that complement-dependent cytotoxicity and inflammatory response pathways decreased in CD55$^+$ B cells (Figure S5e). Flow cytometry showed that the abundance of CD55$^+$ B cells highly varied among tissue origins and individuals (Figure S6a and b). Classical B cell markers were then examined along with CD55, which revealed that intra-tumoural CD55$^+$ B cells mainly exhibited the CD27$^+$ phenotype and lacked CD38 expression (Fig. 5d and Figure S6b). The CD55$^+$ B cells in ESCC were predominantly CD19$^+$CD27$^+$CD20$^+$ memory B cells, although a small fraction of CD55$^+$ B cells had the CD20$^-$CD27$^-$ phenotype (Figure S6c). The expression of CD20 was previously reported to be lost during differentiation at the plasmablast stage,[33] suggesting that the CD19$^+$CD20$^-$CD27$^-$CD55$^+$ cells might be in a transient state to plasmablast cells. Moreover, CD55$^+$ B cells were predominantly IgD$^-$ (Fig. 5e). Regarding cytokine secretion, we observed elevated levels of TGF-β production by CD55$^+$ B cells (Fig. 5e). The analysis by scRNA-seq data further indicated the expression of *TGFB1* in CD55$^+$ B cells (Fig. 5f).

Discrete receptor–ligand interactions between CD55$^+$ B cells and T cells were also predicted by CellphoneDB for responders and non-responders (Table S10). CD55$^+$ B cells evidently interacted with exhausted CD8$^+$ T cells and Tregs in non-responders, compared with responders (Fig. 5g). Notably, *TGFB1* ligand–receptor pairs may mediate crosstalk between CD55$^+$ B cells and Tregs. To directly investigate whether CD55$^+$ B cells enhance Treg differentiation through TGF-β, we purified human CD55$^+$ B cells and other B cells from fresh ESCC specimens using FACS (Figure S6e), followed by *in vitro* co-culture with CD4$^+$T cells in the absence or presence of the TGF- β neutralizer. The results indicated that CD55$^+$ B cells remarkably induced CD4$^+$ T cell differentiation into Treg cells, which was inhibited by TGF-β neutralization (Fig. 5h and Figure S6f). Additionally, the *CD55-ADGRE5* ligand–receptor pair was enriched between CD55$^+$ B cells and exhausted CD8$^+$ T cells, suggesting a potential role for CD55$^+$ B cells in suppressing CD8$^+$ T cells. In comparison with other B cells isolated from the same tumours, CD55$^+$ B cells showed higher capacity to impair the functional ability and expansion of CD8$^+$ T cells from the same patient, reducing their IFN-γ, PRF1, TNF-α, CD107a, and Ki-67 expression. CD55 blockade reinforced the anti-tumour effects of CD8$^+$ T cells (Fig. 5i and Figure S6g). Therefore, our data showed that CD55$^+$ B cells exhibit immune-regulating phenotypes and contribute to immune evasion by facilitating T cell exhaustion.

To confirm whether CD55$^+$ B cells exert immune-regulating effects in vivo, we performed adoptive transfer of T cells and CD55$^+$ or CD55$^-$ B cells into NOD-SCID mice subcutaneously injected with the EC109 cell line (Fig. 5j). Tumour progression was inhibited by T cells co-transferred with CD55$^-$ B cells, but not by T cells co-transferred with CD55$^+$ B cells (Fig. 5k), indicating that CD55$^+$ B cells are an immunosuppressive subset. CD55$^+$ B cell transfer significantly blunted the function of CD8$^+$ T cells, diminishing the secretion of IFN-γ, PRF1, and CD107a in CD8$^+$ T cells, while increasing the proportion of FOXP3$^+$ Tregs (Fig. 5l and Figure S6g). Thus, these results validate the crucial role of CD55$^+$ B cells in immunoevasion and tumour growth in ESCC.

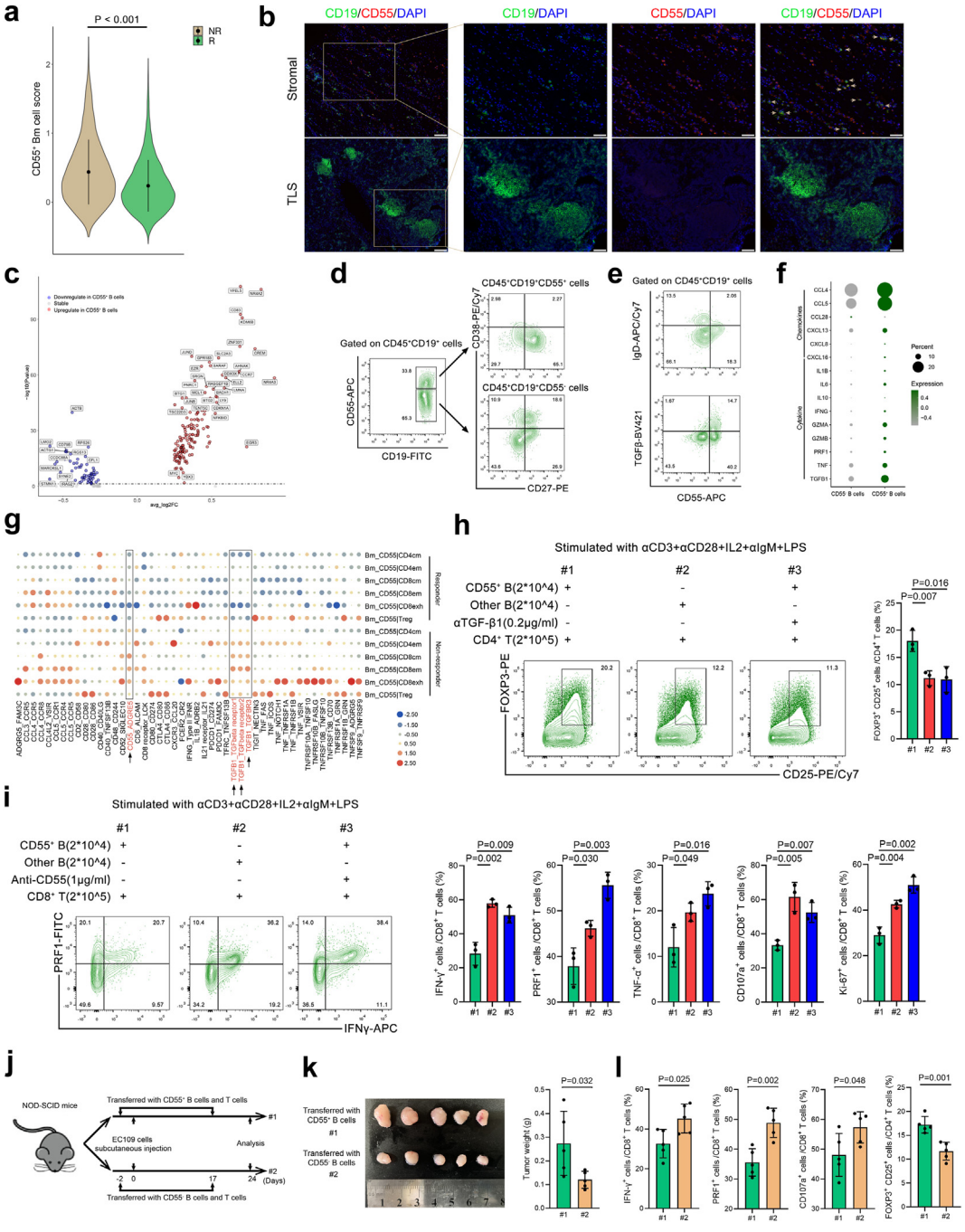

Fig. 5: **CD55$^+$ B cells exhibit immunosuppressing ability and facilitate tumour growth.** **(a)** Comparison of the CD55$^+$ Bm cell signature between B cells from responders and non-responders (Mann–Whitney *U* test). **(b)** Representative immunofluorescence staining for CD19 (green) and CD55 (red) in TLS and stromal of ESCC samples. DAPI staining is shown in blue. Scale bar, 100 μm and 50 μm (zoomed-in image). **(c)** Volcano plot showing differentially expressed genes between CD55$^+$ B cells and CD55$^-$ B cells. **(d** and **e)** Representative flow cytometric plots depicting the phenotype of CD45$^+$CD19$^+$CD55$^+$ B cells defined by markers including CD27, CD38, IgD, and TGF-β. **(f)** Differentially expressed cytokines and chemokines in CD55$^+$ B cells and CD55$^-$ B cells. **(g)** Heatmap showing the strength of interacting pairs between CD55$^+$ Bm cells and T cell clusters in responders and non-responders identified by CellphoneDB. **(h)** The detection of CD25$^+$FOXP3$^+$ Tregs after co-culture of CD4$^+$ T cells and B cells subsets (left) and corresponding statistical analysis (right) (n = 3 per group; Mann–Whitney *U* test). **(i)** The detection of T cell functions after co-culture of CD8$^+$ T cells and B cells subsets (left) and corresponding statistical analysis (right) (n = 3 per group; Mann–Whitney *U* test). **(j)** T cell and B cell subset were transferred to NOD-SCID mice followed by establishment of a subcutaneous ESCC tumour

B cell lineage features predict clinical outcomes

Since the vital roles of intratumoural B cell lineages on the response of ESCC to chemoimmunotherapy were demonstrated, we sought to detect B cell subsets in pre-treatment ESCC samples and explore their potency to predict therapeutic sensitivities. LMO2, CD55, and the B cell marker CD19 were detected in pre-treatment biopsy ESCC tissues (Fig. 6a). The total pre-treatment B cell density was higher in responders, but there was no significant difference in the number of pre-treatment TLSs between responders and non-responders (Figure S7a). Moreover, pre-treatment $LMO2^+$ B cell infiltration increased in responders, and pre-treatment $CD55^+$ B cell density was higher in non-responders, suggesting the predictive effect of B cell subsets (Fig. 6b). Additionally, in multivariate logistic regression analyses, the predictive effect of pre-treatment $CD55^+$ B cells on therapeutic responses appeared to be consistent when adjusting for potential confounders of ESCC (Table S5).

We then analysed a pan-cancer ICB cohort[16,17] to verify the capacity of diverse B cell profiles to predict ICB efficacy. We found that $CD55^+$ Bm cells were associated with suboptimal PFS in the pan-cancer ICB cohort (Fig. 6c). Moreover, high levels of $LMO2^+$ GCB cells predicted significantly prolonged PFS after ICB (Fig. 6d). When integrating $LMO2^+$ GCB cells and TLS into the survival analysis, only patients with both high $LMO2^+$ GCB cells and TLS scores acquired pronounced survival benefits from ICB (Fig. 6d), indicating that TLS may activate the immune response only with the presence of $LMO2^+$ GCB cells. To demonstrate the unique prediction of ICB responses by transcriptomic B cell subset features, this model was further tested in the chemotherapy cohort from ESCC-TCGA. The results of univariable Cox regression showed that the $CD55^+$ Bm score and $LMO2^+$ GCB cell score were not significant prognosticators for patients with ESCC who received adjuvant chemotherapy (Figure S7b). In conclusion, these results showed that the transcriptomic features of B cell lineages might serve as key predictive factors for therapeutic susceptibility.

For comprehensive characterization of B cell lineages, we categorized the patients into different groups based on $CD55^+$ Bm cell, $LMO2^+$ GCB cell and TLS signatures. We performed K-means clustering within the ESCC-TCGA cohort and found four groups of patients with distinct B cell features (Fig. 6e). Tumours from patients in Group 1 exhibited high $CD55^+$ Bm cell infiltration and a sparse abundance of $LMO2^+$ GCB cells and TLS. Survival analysis and log-rank tests demonstrated that Group 1 had the shortest OS (Fig. 6e). Trained with the ESCC-TCGA cohort, we then built a binary classifier using a SVM with linear kernel. Through the SVM model we stratified each patient in the pan-cancer ICB cohort into four groups according to the signature expression of $CD55^+$ Bm cells, $LMO2^+$ GCB cells, and TLS. Likewise, Group 1 showed the shortest progression interval (Fig. 6f), even when compared to that of Group 2, which included patients with high $CD55^+$ Bm cells and high $LMO2^+$ GCB cells. Taken together, these results demonstrate that risk grouping based on transcriptomic B cell lineage features may serve as a useful predictor of the clinical benefits of immunotherapy.

We further validate our findings among patients receiving PD-1 inhibitors plus nab-paclitaxel and platinum-based chemotherapy in our cohort. In pre-treatment samples, the responders carried significantly higher indel counts and deficient MMR signature scores comparing to non-responders (Figure S8a and b). Comparisons of DDR pathway alternations also revealed higher frequencies of MMR alternations in responsive tumours before treatments (Figure S8b). Of note, pre-treatment indel-derived neoantigens were only carried by ESCC with MMR alternations (Figure S8c).

Regarding the B cell features, analysis through scRNA-seq data revealed increased proportion of Bm_CD55 cells among total B cells in tumors from non-responders after therapy (Figure S8e). In pre-treatment samples, $CD55^+$ B cell infiltration was observed to increase in non-responders, while $LMO2^+$ B cell density was higher in responders (Figure S8g). Overall, indel counts, MMR alternations and recognised B cell features in this study are correlated with the responses of neoadjuvant PD-1 inhibitors plus nab-paclitaxel and platinum-based chemotherapy in ESCC.

Association of B cell heterogeneity with genome characteristics of ESCC

Genomic features have been established as key indicators of therapeutic benefits in ESCC.[34] To investigate whether B cell features were associated with somatic genomic variations, we followed a pathway-focused approach to identify enriched genomic alterations. By examining the association between pathway alternations and B cell feature groupings, we found an exclusion of alternations in MMR pathways in patients from Group 1 (Fig. 6g), characterised by tumours harbouring predominantly $CD55^+$ Bm cells and a low proportion of $LMO2^+$ GCB cells. This supported the link between

model. **(k)** Tumour weights after adoptive transfer and subcutaneous ESCC tumour model construction (n = 5 per group; Mann–Whitney *U* test). **(l)** Comparison of intra-tumoral $CD8^+$ T cell functions and Treg proportions after adoptive transfer and subcutaneous ESCC tumour model construction (n = 5 per group; Mann–Whitney *U* test). P values are indicated in the figure. Error bars in bar plots represent the standard deviation.

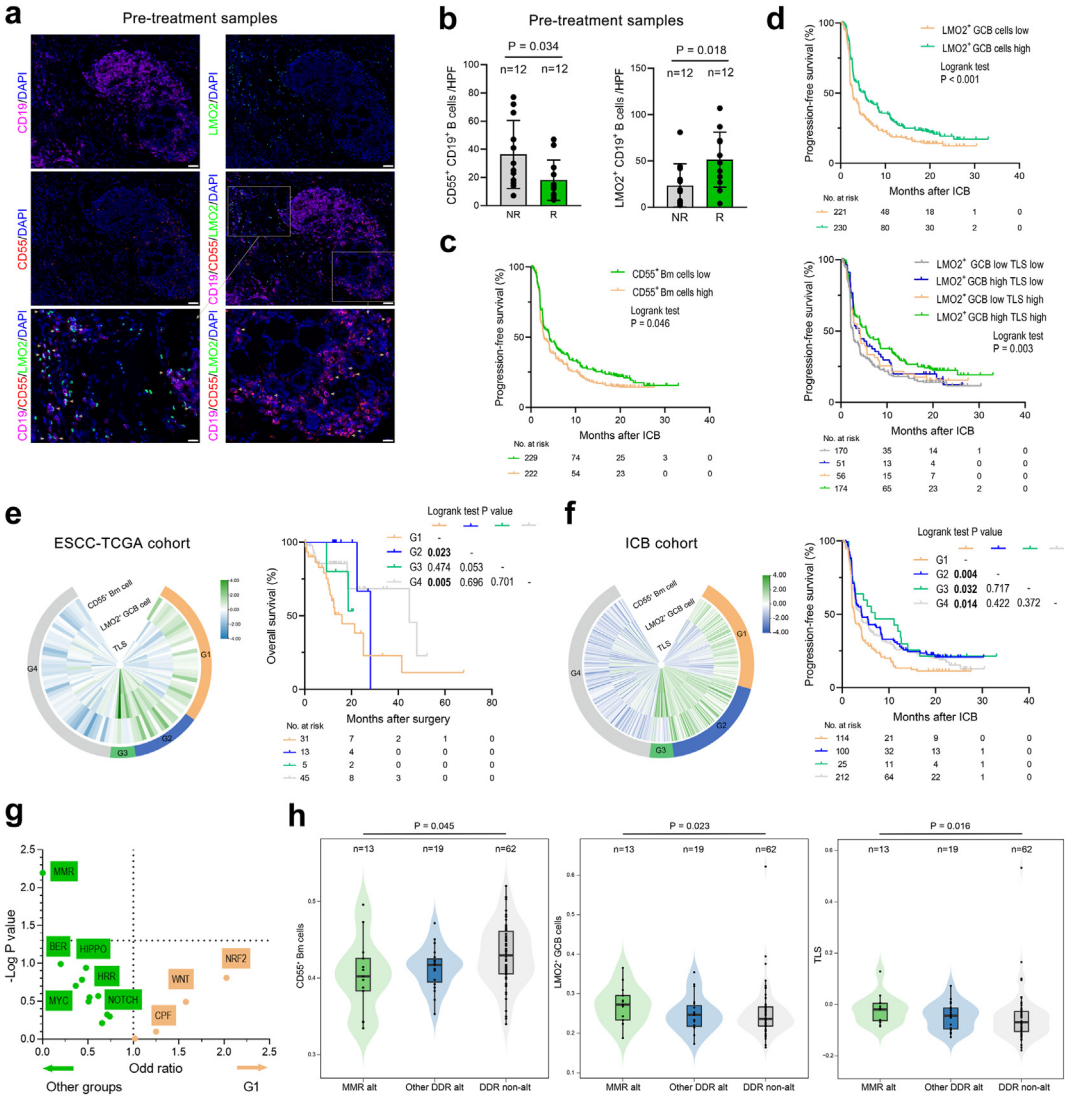

Fig. 6: **B cell linage features predict clinical outcomes and correlate with MMR alteration status.** **(a)** Representative immunofluorescence staining for CD19 (magenta), LMO2 (green) and CD55 (red) in pre-treatment ESCC tissues. DAPI staining is shown in blue (left). Scale bar, 50 μm and 20 μm (zoomed-in image). **(b)** Comparison of infiltrating $LMO2^+$ B cells and $CD55^+$ B cells between responders and non-responders before treatment (right; Mann–Whitney *U* test). **(c)** Survival curves generated for $CD55^+$ Bm cell signatures in ICB cohort (n = 451; log-rank test). **(d)** Progression-free survival curves generated for $LMO2^+$ GCB cell signatures (upper) and combined with TLS signatures (lower) in the ICB cohort (n = 451; log-rank test). **(e)** Circular heatmap showing risk grouping based on B cell lineage features in the ESCC-TCGA cohort (the outer circle represents scaled $CD55^+$ Bm cell expression, middle circle represents scaled $LMO2^+$ GCB cell expression, and inner circle represents scaled TLS expression; left) and overall survival curves generated for risk groups (n = 94; log-rank test; right). **(f)** Risk grouping based on B cell lineage features in the ICB cohort (the outer circle represents scaled $CD55^+$ Bm cell expression, middle circle represents scaled $LMO2^+$ GCB cell expression, and inner circle represents scaled TLS expression; left) and progression-free survival curves generated for risk groups (log-rank test; right). **(g)** Volcano plot showing the odd ratios of frequencies of pathway alternations in different risk groups calculated by the univariate logistic regression model in the ESCC-TCGA cohort. **(h)** Comparison of $CD55^+$ Bm cells, $LMO2^+$ GCB cells, and TLS according to MMR and DDR status (Mann–Whitney *U* test). The number of samples and P values are indicated directly in the figure. Error bars in bar plots represent the standard deviation.

MMR pathway alternations and B cell lineage features. Moreover, $CD55^+$ Bm cells were diminished while $LMO2^+$ GCB cells and TLS signatures were elevated in tumours with MMR alterations from the ESCC-TCGA cohort (Fig. 6h). In summary, we have provided evidence that MMR pathway alternations may correlate with B cell lineages, thus contributing to ICB susceptibility.

Discussion

Neoadjuvant anti-PD-1-based chemoimmunotherapy has provided additional treatment opportunities for patients with locally advanced ESCC, resulting in prolonged survival. However, therapeutic sensitivity varies substantially among individuals, and the mutational and immunological determinants of these responses remain unknown. In this study, we demonstrated that tumours with high indel mutations exhibited robust responses to combination therapy. Given the frameshift nature of indel mutations, which create novel open reading frames and mutagenic peptides, indels may induce a vigorous immune response and exaggerate immunotherapy efficacy.[19,35] We further identified that ESCC with mutational MMR alternations was more sensitive to neoadjuvant chemoimmunotherapy and exhibited vigorous anti-tumour immune response with increased infiltration of B cells. As speculated, these MMR-alternated tumours contained more indel-derived MANAs, which exhibit predictive potential for the therapeutic response.

Through scRNA-seq, we found non-responding tumours were enriched with Tregs and $CD55^+$ Bm cells, whereas tumours from responders possessed a high abundance of naïve B and GCB cells. Prior bulk RNA-seq and scRNA-seq analyses have demonstrated the key role of intra-tumoural B cells in responding to tumour development and influencing ICB sensitivity in various tumours.[36–39] In the present study, dichotomous B cell lineages were observed in post-treated ESCC, with distinctive expression of *LMO2* or *CD55*, consistent with a recent report showing that CD55 repression is required to induce GCB cells.[32] After somatic hypermutation and affinity maturation, GCB cells are crucial for antigen presentation via MHC II and T-cell activation within the TLS.[9,40] Our results indicate that $LMO2^+$ GCB cells play key roles in mounting anti-tumour immune responses, and only TLSs with sufficient $LMO2^+$ GCB cell infiltration may demonstrate a clinical benefit from immunotherapy.

In addition, TLS is highly heterogeneous and can evolve through different stages of maturation. In immature TLSs, B cells are aggregated, but neither B cell follicles nor follicular dendritic cells are present and memory B cells therein do not further mature, often acquiring immunosuppressive activities.[41] Here, we identified a regulatory cluster of $CD55^+$ Bm cells within ESCC, expressing preponderated transcriptomic signatures of memory B cell activation, which are involved in immune regulation.[42–44] Within the TME of ESCC, $CD55^+$ B cells were detected outside of the GC and TLS, implicating that $CD55^+$ memory B cells were generated from a lineage other than the GCB lineage. In addition to complement regulation, CD55 was reported to bind to ADGRE5, an EGF-TM7 receptor, and regulate T cell activation, leading to the induction of IL-10-producing Tr1 regulatory cells.[45–47] Herein, the CD55-ADGRE5 interactions between $CD55^+$ B cells and exhausted $CD8^+$ T cells were predicted. We demonstrated that $CD55^+$ B cells may directly inhibit the anti-tumour effects of $CD8^+$ T cells and blocking CD55 reinforced $CD8^+$ T cell activation. Our study thus offers a new perspective to understand the anti-tumour mechanisms of CD55 inhibitors, warranting further exploration of the application of B cell-specific CD55 inhibitors.

After validating that the pre-treatment and post-treatment levels of intratumoural $LMO2^+$ B cells and $CD55^+$ B cells may distinguish responses to combination therapy in our cohort, transcriptomic signatures were then designed to infer comprehensive B cell lineage features in bulk transcriptomes and examined to predict ICB responsiveness. We found that the abundance of $LMO2^+$ GCB cells was associated with better prognosis in patients treated with ICB, whereas patients with high $CD55^+$ Bm cell scores hardly benefited from ICB. Additionally, a group of patients with high $CD55^+$ Bm cells and low $LMO2^+$ GCB cells plus TLS was stratified for the worst clinical outcomes in both the ESCC-TCGA and ICB cohorts, exhibiting the prognostic and predictive value of B cell features. Moreover, tumours with MMR alternations harboured less $CD55^+$ Bm cells but more $LMO2^+$ GCB cells and TLS, suggesting a reciprocal relationship between TME and genomic profiling within ESCC. We plan to follow up with this cohort with respect to the subsequent treatment status and the 3-year PFS to validate the prognostic value of the recognized features for ESCC treated with the combination regimen.

As limitations, this study was observational in nature and limited in sample size. In addition, the variation of therapy regimen may affect therapeutic outcomes. Reports have been made to demonstrate the better efficacy of nab-paclitaxel comparing to solvent-based paclitaxel.[48] Due to the small sample size, the discrepancy of therapeutic efficacy of different formulations of paclitaxel was unidentifiable in this study. We further examined and confirmed the correlation of indel counts, MMR alternations, and B cell features with therapeutic responses in patients receiving neoadjuvant PD-1 inhibitors plus nab-paclitaxel and platinum-based chemotherapy. Moreover, our understanding of the mechanisms underlying the biological effects of tumour molecular profiles on TME remains insufficient. In future studies, we plan to conduct biochemical experiments to investigate the molecular mechanisms of MMR alternations in tumour cells that harness immune responses. Furthermore, prospective clinical trials with homogeneous immunotherapy and chemotherapy regimens are needed to validate the prognostic value of recognised genomic and immune features in this study. We also expect to expand the cohorts and integrate lymph node and peripheral blood samples into examinations from patients receiving single-agent therapy to provide a more thorough understanding of the

dynamics of immune profiling for the selection of patients with ESCC to undergo immunotherapies.

Contributors

H. Zhang, H. Wen, Y. Zhang, Y. Guo for data acquisition, analysis and interpretation of data, statistical analysis and writing of the draft; Q. Zhu, F. Xu, T. Ma, Z. Wang, X. Zhao, Y. Ji for technical and material resource support; C. Lu, Y. Chu, R. Liu for management of research activities and review of the manuscript; D. Ge, J. Gu, and R. Liu for conceptualization and design of the study, funding acquisition and study supervision. H. Zhang, J. Gu, and R. Liu have accessed and verified the underlaying data and were responsible for the decision to submit the manuscript. All authors read and approved the final manuscript.

Data sharing statement

Whole-exome sequencing data reported in this paper have been deposited in the Genome Variation Map in National Genomics Data Center, Beijing Institute of Genomics, Chinese Academy of Sciences and China National Center for Bioinformation (https://ngdc.cncb.ac.cn), under accession number GVM000494. Single-cell RNA sequencing data generated by this study have been deposited in the Chinese national genomics data center, under accession number OMIX003024. Raw sequencing data was deposited in the National Genomics Data Center, under accession number HRA006065. Because of patient privacy constraints, raw data are under controlled access and available upon request to corresponding authors. Additional data related to this paper may be requested from the authors. Any additional information required to reanalyse the data reported in this paper is available from the lead contact upon request. No custom code was generated in this study.

Declaration of interests

The authors declare no competing interests.

Acknowledgements

This work was supported by the National Science Foundation of China (82373371, 82330053), the Program for professor of special appointment (Eastern Scholar) at Shanghai Institutions of Higher Learning, National Science and Technology Major Project of China (2023YFA1800204, 2020YFC2008402), and Science and Technology Commission of Shanghai Municipality (22ZR1410700 and 20ZR1410800).

Appendix A. Supplementary data

Supplementary data related to this article can be found at https://doi.org/10.1016/j.ebiom.2024.104971.

References

1 Kojima T, Shah MA, Muro K, et al. Randomized phase III KEYNOTE-181 study of pembrolizumab versus chemotherapy in advanced esophageal cancer. *J Clin Oncol*. 2020;38(35):4138–4148.
2 Sun JM, Shen L, Shah MA, et al. Pembrolizumab plus chemotherapy versus chemotherapy alone for first-line treatment of advanced oesophageal cancer (KEYNOTE-590): a randomised, placebo-controlled, phase 3 study. *Lancet*. 2021;398(10302):759–771.
3 Luo H, Lu J, Bai Y, et al. Effect of camrelizumab vs placebo added to chemotherapy on survival and progression-free survival in patients with advanced or metastatic esophageal squamous cell carcinoma: the ESCORT-1st randomized clinical trial. *JAMA*. 2021;326(10):916–925.
4 Lu Z, Wang J, Shu Y, et al. Sintilimab versus placebo in combination with chemotherapy as first line treatment for locally advanced or metastatic oesophageal squamous cell carcinoma (ORIENT-15): multicentre, randomised, double blind, phase 3 trial. *BMJ*. 2022;377:e068714.
5 Janjigian YY, Shitara K, Moehler M, et al. First-line nivolumab plus chemotherapy versus chemotherapy alone for advanced gastric, gastro-oesophageal junction, and oesophageal adenocarcinoma (CheckMate 649): a randomised, open-label, phase 3 trial. *Lancet*. 2021;398(10294):27–40.
6 Liu J, Yang Y, Liu Z, et al. Multicenter, single-arm, phase II trial of camrelizumab and chemotherapy as neoadjuvant treatment for locally advanced esophageal squamous cell carcinoma. *J Immunother Cancer*. 2022;10(3):e004291.
7 Yan X, Duan H, Ni Y, et al. Tislelizumab combined with chemotherapy as neoadjuvant therapy for surgically resectable esophageal cancer: a prospective, single-arm, phase II study (TD-NICE). *Int J Surg*. 2022;103:106680.
8 Bruno TC, Ebner PJ, Moore BL, et al. Antigen-presenting intratumoral B cells affect CD4(+) TIL phenotypes in non-small cell lung cancer patients. *Cancer Immunol Res*. 2017;5(10):898–907.
9 Gunderson JA, Rajamanickam V, Bui C, et al. Germinal center reactions in tertiary lymphoid structures associate with neoantigen burden, humoral immunity and long-term survivorship in pancreatic cancer. *Oncoimmunology*. 2021;10(1):1900635.
10 Helmink BA, Reddy SM, Gao J, et al. B cells and tertiary lymphoid structures promote immunotherapy response. *Nature*. 2020;577(7791):549–555.
11 Mandard AM, Dalibard F, Mandard JC, et al. Pathologic assessment of tumor regression after preoperative chemoradiotherapy of esophageal carcinoma. Clinicopathologic correlations. *Cancer*. 1994;73(11):2680–2686.
12 Abnet CC, Arnold M, Wei WQ. Epidemiology of esophageal squamous cell carcinoma. *Gastroenterology*. 2018;154(2):360–373.
13 Alexandrov LB, Kim J, Haradhvala NJ, et al. The repertoire of mutational signatures in human cancer. *Nature*. 2020;578(7793):94–101.
14 Alam A, Comer S, Levanduski E, Dey P. Isolation and adoptive transfer of innate lymphoid cells 2 to a recipient mouse model of PDAC. *STAR Protoc*. 2022;3(3):101563.
15 Xia Y, Sandor K, Pai JA, et al. BCL6-dependent TCF-1(+) progenitor cells maintain effector and helper CD4(+) T cell responses to persistent antigen. *Immunity*. 2022;55(7):1200–1215.e6.
16 Mariathasan S, Turley SJ, Nickles D, et al. TGFβ attenuates tumour response to PD-L1 blockade by contributing to exclusion of T cells. *Nature*. 2018;554(7693):544–548.
17 Banchereau R, Leng N, Zill O, et al. Molecular determinants of response to PD-L1 blockade across tumor types. *Nat Commun*. 2021;12(1):3969.
18 Cheong JH, Wang SC, Park S, et al. Development and validation of a prognostic and predictive 32-gene signature for gastric cancer. *Nat Commun*. 2022;13(1):774.
19 Turajlic S, Litchfield K, Xu H, et al. Insertion-and-deletion-derived tumour-specific neoantigens and the immunogenic phenotype: a pan-cancer analysis. *Lancet Oncol*. 2017;18(8):1009–1021.
20 Zhang K, Hong X, Song Z, et al. Identification of deleterious NOTCH mutation as novel predictor to efficacious immunotherapy in NSCLC. *Clin Cancer Res*. 2020;26(14):3649–3661.
21 Wang Z, Zhao J, Wang G, et al. Comutations in DNA damage response pathways serve as potential biomarkers for immune checkpoint blockade. *Cancer Res*. 2018;78(22):6486–6496.
22 Sanchez-Vega F, Mina M, Armenia J, et al. Oncogenic signaling pathways in the cancer genome Atlas. *Cell*. 2018;173(2):321–337.e10.
23 Thorsson V, Gibbs DL, Brown SD, et al. The immune landscape of cancer. *Immunity*. 2018;48(4):812–830.e14.
24 Trotter TN, Shuptrine CW, Tsao LC, et al. IL26, a noncanonical mediator of DNA inflammatory stimulation, promotes TNBC engraftment and progression in association with neutrophils. *Cancer Res*. 2020;80(15):3088–3100.
25 Munn DH, Sharma MD, Johnson TS. Treg destabilization and reprogramming: implications for cancer immunotherapy. *Cancer Res*. 2018;78(18):5191–5199.
26 De Silva NS, Klein U. Dynamics of B cells in germinal centres. *Nat Rev Immunol*. 2015;15(3):137–148.
27 King HW, Orban N, Riches JC, et al. Single-cell analysis of human B cell maturation predicts how antibody class switching shapes selection dynamics. *Sci Immunol*. 2021;6(56):eabe6291.
28 Natkunam Y, Zhao S, Mason DY, et al. The oncoprotein LMO2 is expressed in normal germinal-center B cells and in human B-cell lymphomas. *Blood*. 2007;109(4):1636–1642.
29 Cabrita R, Lauss M, Sanna A, et al. Tertiary lymphoid structures improve immunotherapy and survival in melanoma. *Nature*. 2020;577(7791):561–565.
30 Petitprez F, de Reyniès A, Keung EZ, et al. B cells are associated with survival and immunotherapy response in sarcoma. *Nature*. 2020;577(7791):556–560.

31 Siliņa K, Soltermann A, Attar FM, et al. Germinal centers determine the prognostic relevance of tertiary lymphoid structures and are impaired by corticosteroids in lung squamous cell carcinoma. *Cancer Res*. 2018;78(5):1308–1320.
32 Cumpelik A, Heja D, Hu Y, et al. Dynamic regulation of B cell complement signaling is integral to germinal center responses. *Nat Immunol*. 2021;22(6):757–768.
33 Jego G, Bataille R, Pellat-Deceunynck C. Interleukin-6 is a growth factor for nonmalignant human plasmablasts. *Blood*. 2001;97(6):1817–1822.
34 Cui Y, Chen H, Xi R, et al. Whole-genome sequencing of 508 patients identifies key molecular features associated with poor prognosis in esophageal squamous cell carcinoma. *Cell Res*. 2020;30(10):902–913.
35 Maby P, Tougeron D, Hamieh M, et al. Correlation between density of CD8+ T-cell infiltrate in microsatellite unstable colorectal cancers and frameshift mutations: a rationale for personalized immunotherapy. *Cancer Res*. 2015;75(17):3446–3455.
36 Griss J, Bauer W, Wagner C, et al. B cells sustain inflammation and predict response to immune checkpoint blockade in human melanoma. *Nat Commun*. 2019;10(1):4186.
37 Sharonov GV, Serebrovskaya EO, Yuzhakova DV, Britanova OV, Chudakov DM. B cells, plasma cells and antibody repertoires in the tumour microenvironment. *Nat Rev Immunol*. 2020;20(5):294–307.
38 Ruffin AT, Cillo AR, Tabib T, et al. B cell signatures and tertiary lymphoid structures contribute to outcome in head and neck squamous cell carcinoma. *Nat Commun*. 2021;12(1):3349.
39 Gu S, Qian L, Zhang Y, et al. Significance of intratumoral infiltration of B cells in cancer immunotherapy: from a single cell perspective. *Biochim Biophys Acta Rev Cancer*. 2021;1876(2):188632.
40 Holmes AB, Corinaldesi C, Shen Q, et al. Single-cell analysis of germinal-center B cells informs on lymphoma cell of origin and outcome. *J Exp Med*. 2020;217(10):e20200483.
41 Fridman WH, Meylan M, Petitprez F, Sun CM, Italiano A, Sautès-Fridman C. B cells and tertiary lymphoid structures as determinants of tumour immune contexture and clinical outcome. *Nat Rev Clin Oncol*. 2022;19(7):441–457.
42 Zhang Y, Chen H, Mo H, et al. Single-cell analyses reveal key immune cell subsets associated with response to PD-L1 blockade in triple-negative breast cancer. *Cancer Cell*. 2021;39(12):1578–1593.e8.
43 Edry E, Melamed D. Class switch recombination: a friend and a foe. *Clin Immunol*. 2007;123(3):244–251.
44 Viant C, Wirthmiller T, ElTanbouly MA, et al. Germinal center-dependent and -independent memory B cells produced throughout the immune response. *J Exp Med*. 2021;218(8):e20202489.
45 Sutavani RV, Bradley RG, Ramage JM, Jackson AM, Durrant LG, Spendlove I. CD55 costimulation induces differentiation of a discrete T regulatory type 1 cell population with a stable phenotype. *J Immunol*. 2013;191(12):5895–5903.
46 Capasso M, Durrant LG, Stacey M, Gordon S, Ramage J, Spendlove I. Costimulation via CD55 on human CD4+ T cells mediated by CD97. *J Immunol*. 2006;177(2):1070–1077.
47 Spendlove I, Sutavani R. The role of CD97 in regulating adaptive T-cell responses. *Adv Exp Med Biol*. 2010;706:138–148.
48 Socinski MA, Bondarenko I, Karaseva NA, et al. Weekly nab-paclitaxel in combination with carboplatin versus solvent-based paclitaxel plus carboplatin as first-line therapy in patients with advanced non-small-cell lung cancer: final results of a phase III trial. *J Clin Oncol*. 2012;30(17):2055–2062.